Radio Science, Volume ???, Number , Pages 1–21,

Observability of Ionospheric Space-Time Structure with ISR: A simulation study

John Swoboda,[1] Joshua Semeter,[1] Philip Erickson[2]

[1]Department of Electrical & Computer Engineering, Boston University, Boston, Massachusetts, USA.

[2]Haystack Observatory, Massachusetts Institute of Technology, Westford, Massachusetts, USA.

As with any sensing modality incoherent scatter radar (ISR) has inherent errors and uncertainty in its measurements. A number of theoretical aspects behind these errors have been documented in the literature, which leads to a trade off between spatial and temporal resolution and statistical accuracy.

Resource allocation and experiment design. Understand degrees of freedom in design.

The recent application of phased array antennas with pulse to pulse steering allow for greater flexibility in processing along with making it is now possible to create full volumetric reconstructions of plasma parameters. These phased array systems are used heavily in the high latitude region of the ionosphere, which can have plasma phenomena that is highly variable in space and time. In order to develop an experiment to observe the plasma phenomena researchers have to wade through a large number of degrees of freedom. In order to properly allocate resources in some cases researchers may need to simulate the experiment.

This publication will show a simulator that can take a field of plasma parameters and create ISR data at the IQ level and then process it to show a possible reconstruction of the parameters field. This simulator can be used to create ISR data to test new algorithms to better reconstruct the plasma parameter field. It can also give researchers a new tool that can assist them

in the set up their experiments. This simulation will overall give a full forward model description of the ISR reconstruction.

1. Introduction

Incoherent scatter radar is an important diagnostic for the ionosphere in that it can give direct measurements of the intrinsic plasma parameters [*Dougherty and Farley*, 1960; *Farley et al.*, 1961; *Dougherty and Farley*, 1963; *Hagfors*, 1961]. As with all diagnostic tools it has associated with it sources of errors which include time and spatial ambiguities [*Farley*, 1969a, b; *Hysell et al.*, 2008; *Swoboda et al.*, 2015].

One unique aspect of ISR is that inherent random fluctuations of the plasma are used to create these measurements. These fluctuations are used by creating second order statistics from a scattered signal, specifically an autocorrelation function (ACF) [*Farley*, 1969a]. The statistical nature of the target itself yields the requirement of averaging numerous realizations of the ACF to reduce the variance of the estimate. This forces the assumption of stationarity for a space-time cell, which may not be true. In the end this creates a trade-off between space-time resolution and the variance of the measurements.

Application of electronically steerable array (ESA) technology to ISR has been a recent advancement for the community. ISRs such as these, like the Advanced Modular Incoherent Scatter (AMISR) systems, have already been deployed in Poker Flat Alaska and Resolute Bay Canada [*Nicolls and Heinselman*, 2007; *Dahlgren et al.*, 2012a]. These ESA based systems are seen as the future of the ISR sensor modality due to the flexibility in beam steering, processing and other aspects over dish based systems. The next step in the evolution of these systems is expected to be the EISCAT-3D project, which will have a number of enhancements such as multi-static

processing capability and be able to receive and process data from each phased array element by default.

One benefit of ESA based ISR is that volumetric reconstructions of plasma parameters can be created [*Semeter et al.*, 2009; *Nicolls and Heinselman*, 2007; *Dahlgren et al.*, 2012a]. These systems also have ben used to reconstuct full vector parameters using estimates of the ion velocity which can be determined using the Doppler shift of spectra [*Butler et al.*, 2010; *Nicolls et al.*, 2014]. Still it has been shown that the volumetric reconstructions can yield measurements with a high degree of ambiguity [*Dahlgren et al.*, 2012b]. Similar type of ambiguities have been seen when using systems with a dish antenna as well. In *Semeter et al.* [2005] the authors to show an undersampling in the horizontal dimension, but are able to compensate by changing processing parameters.

With these new capabilities for the ISR community a discussion of the possible sources of uncertainty and error is needed. These sources of error and ambiguity though are difficult understand in the context of experiment design. With that in mind it may be useful to simulate the ISR measurement process before an experiment is attempted. With that in mind this paper will show how one could simulate an experiment, the outline of this is a follows. After listing the possible sources of error and ambiguity in ISR our simulation method will be detailed. After which a number of examples of the simulator will be shown. These example range from a stationary column of enhanced electron density to the output of a self-consistent multi-fluid ionosphereic model [*Zettergren and Semeter*, 2012]. These examples will

illustrate how one could develop their experiments in a systematic way in order make measurements that best reflect the physics present in the ionosphere.

2. ISR Errors

In this section the main sources of ISR errors will be discussed. The first part of this discussion will cover the statistical errors that arise from the ISR process. After that the errors from the spatial and temporal ambiguity of ISR systems will be shown. This in the end will lead to trade offs that the experiment designer will have to face.

2.1. Statistical Errors

To measure the plasma parameters ISR takes advantage of the random fluctuations of electron density in the ionosphere. The theory of how the plasma parameters impact the statistics of these fluctuations have been discussed since the first use of this sensor modality [*Gordon*, 1958; *Dougherty and Farley*, 1960; *Farley et al.*, 1961; *Dougherty and Farley*, 1963; *Hagfors*, 1961], and even as recent as 2011 there have been new formulations of this theory [*Kudeki and Milla*, 2011; *Milla and Kudeki*, 2011].

The two main sources of statistical error will covered here are the random fluctuations from the electron density and noise from within the sensor itself. There are other sources of statistical error including sky noise and coherent scatter from other targets.

The raw incoherent scatter signal is itself is a random process. As such it is necessary to average samples of an estimator for autocorrelation or spectrum [*Diaz et al.*, 2008]. An easy rule of thumb to understand how the error will reduce can be seen in *Farley* [1969a],

$$\left\langle \left| \hat{R}(\tau) - R(\tau) \right|^2 \right\rangle \propto \frac{1}{\sqrt{J}}, \tag{1}$$

where $R(\tau)$ is the ACF as a function of lag τ, $\hat{R}(\tau)$ is its estimate and J is the number of samples or pulses averaged together to create the estimate.

The variance of this signal is further degraded once noise from the sensor is added. The noise from the sensor is assumed to be uncorrelated to the signal. Thus the error from the noise can simply be added to the error from the inherent fluctuations in the signal.

2.2. Space-Time Errors

The errors created through the ambiguity function lead to a blurring or averaging of ACFs from different points in time and space. This is similar to a blurring operator one might see in a camera or numerous other types of sensors. With ISR this can be more problematic due to the non-linear fitting step.

The space-time ambiguity, $L(\tau_s, \mathbf{r}_s, t_s, \tau, \mathbf{r}, t)$, is the kernel of Fredholm integral equation of the first kind operating on the ACF, $R(\tau, \mathbf{r}, t)$, which can change over space, $\mathbf{r}$, and time t. which can be represented as follows,

$$\rho(\tau_s, \mathbf{r}_s, t_s) = \int L(\tau_s, \mathbf{r}_s, t_s, \tau, \mathbf{r}, t) R(\tau, \mathbf{r}, t) dV dt d\tau, \tag{2}$$

where the subscript s represents the same variable but now discretely sampled by the radar.

The kernel is a separable function when the spatial coordinates are spherical, where (r, θ, ϕ) represent, range, azimuth and elevation respectively. This the changes Equation 2 as follows,

$$\rho(\tau_s, \mathbf{r}_s, t_s) = \int G(t_s, t) F(\theta_s, \phi_s, \theta, \phi) W(\tau_s, r_s, \tau, r) R(\tau, \mathbf{r}, t) dV dt d\tau, \tag{3}$$

where $G(t_s, t)$ is the kernel for the time dimension, $F(\theta_s, \phi_s, \theta, \phi)$ is radar beam shape which acts as a kernel in azimuth and elevation, and $W(\tau_s, r_s, \tau, r)$ which is the range ambiguity function which acts as a kernel along range r and lag τ. The derivation of this operator can be seen in *Swoboda et al.* [2015].

These two sources of error create a significant trade off between statistical variation of the signal and spatial and temporal resolution of the signal. In order to reduce the statical fluctuations in the signal pulses need to be averaged together. This is necessary even for the case where there is no noise, in a sense the infinite signal to noise ratio (SNR) case. This integration is mainly done over time but can be done over space as well. For phased array systems this mixture of spatial and temporal averaging can be done by averaging together beams. This though will reduce cross range resolution but could possibly improve temporal resolution. It is for this reason

these types of trade offs can best be explored through simulation, which will be covered in the following sections.

3. Simulator

The following section will detail the processing steps in the ISR simulator. The first part will detail the creation of the inphase and quadrature data (IQ data). The next will detail the processing used to create the estimates of the ACFs, which will also be referred to as lag products.

3.1. Inputs

The simulator takes as input a discretized set of ionosphere parameters in Cartesian coordinates and which can change with time. Each point in time and space has a set of parameters that allow it to make an ISR spectrum. For details on creating these spectra see [*Kudeki and Milla*, 2011] and [*Milla and Kudeki*, 2011]. The spectra are then created so every point in space and time will have its own intrinsic ISR spectrum. The radar will then act on these spectrums as a linear operator and average them together in time and space using the beam patterns and pulse pattern. This is an acceptable because spatial correlations between the electron density fluctuations will be on the order of the Debye length *Farley* [1969a],

3.2. IQ Data Creation

The IQ data is created by taking a complex white Gaussian noise process and shaping the spectrum using a filter. Each point in space and time will have a sep-

arate noise plant and filter which is derived from the plasma and radar parameters parameters, like that seen in Figure 1.

The radar samples the space in a spherical coordinate system with discrete range and beam positions. For each range gate and beam the different spectrums are averaged together together. In range this is simply a window the length of a range gate. Across the azimuth and elevation space the beam pattern for the system is used. In order to calculate the beam pattern for the AMISR system the method detailed in the appendix of [*Swoboda et al.*, 2015]. The entire process of the spatial sample is shown in the simplified diagram in Figure 2.

Once the spectrum has been created the filter, $H_m(\omega)$, is created by simply taking the square root of the spectrum, $S_m(\omega|\,\boldsymbol{\theta})$

$$H_m(\omega) = \sqrt{S_m(\omega|\,\boldsymbol{\theta})}. \tag{4}$$

The term $\boldsymbol{\theta}$ refers to the different plasma and system parameters needed to make the spectrum. Complex white Gaussian noise, CWGN, ($w(k) \sim CN(0, \mathbf{I})$) is then pushed though each of the filters and then windowed by the pulse creating the following:

$$y_m(k) = s(k)\left[h_m(k) * w(k)\right], \tag{5}$$

where $s(k)$ is the pulse shape. The application of this filter is actually done in the frequency domain. This is possible because the Discrete Fourier Transform (DFT) of a vector of CWGN is also CWGN. The only difference is that there is a change

in the variance, which is tied to the number of points used in the DFT [*Kay*, 1993]. With this in mind Equation 5 can be implemented as the following,

$$y_m(k) = s(k) \sum_{i=0}^{K-1} e^{j\omega_i k} \left[\sqrt{S_m(\omega_i | \, \boldsymbol{\theta})} w(\omega_i) \right], \tag{6}$$

where ω_i is the frequency variable, $w(\omega_i) \sim CN(0, \mathbf{I})$ and K is the number of points used for the DFT [*Mitchell and Mcpherson*, 1981].

After the data for each range gate $y_m(k)$ is created the power of the return is calculated

$$P_r = \frac{cG\lambda^2}{2(4\pi)^2} \frac{P_t}{R^2} \frac{\sigma_e N_e}{(1 + k^2\lambda_D^2), (1 + k^2\lambda_D^2 + T_r)} \tag{7}$$

where P_r is the power received, c is the speed of light, G is the gain of the antenna, P_t is the power of the transmitter, σ_e is the electron radar cross section, k is the wavenumber of the radar, λ_D is the Debye length, N_e is the electron density and T_r is the electron to ion temperature ratio.

Once the power has been calculated for each range all of the data is delayed and summed together so as to model the arrival of the radar return at the receive:

$$x(n) = \sum_{m=0}^{M-1} \alpha(m) y_m(n - m), \tag{8}$$

where $\alpha(m) = \sqrt{P_r(m)}/\hat{\sigma_y}$ and $\hat{\sigma_y}$ is the estimate of the standard deviation of $y_m(k)$. Lastly, to model the inherent noise in the radar and environment more complex Gaussian noise is added

$$x_f(n) = x(n) + \sqrt{\frac{k_b T_{sys} B}{2}} w(n), \quad w(n) \sim CN(0,1) \tag{9}$$

where k_b is Boltzmann's constant, T_{sys} is the system temperature and B is the system bandwidth. A full diagram of the model can be seen in Figure 3.

3.3. ACF Estimation

After the IQ data has been created it is processed to create estimates of the ACF at desired points of space. This type of processing has been detailed and analyzed in [*Farley*, 1969a] and in other publications. This processing follows a flow chart seen in Figure 4.

The lag product formation is an initial estimate of the autocorrelation function. The sampled I/Q can be represented as $x(n) \in \mathbb{C}^N$ where N is the number of samples in an inter pulse period. For each range gate $m \in 0, 1, ...M-1$ an autocorrelation is estimated for each lag of $l \in 0, 1..., L-1$. To get better statistics this operation is performed for each pulse $j \in 0, 1, ...J-1$ and then summed over the J pulses. The entire operation to form the initial estimate of $\hat{R}(m,l)$ can be seen in Equation 12:

$$\hat{R}(m,l) = \sum_{j=0}^{J-1} x(m - \lfloor l/2 \rfloor, j) x^*(m + \lceil l/2 \rceil, j). \tag{10}$$

The case shown in Equation 12 is a centered lag product, other types of lag products calculations are available but generally a centered product is used. In the centered lag product case range gate index m and sample index n can be related by $m = n - \lfloor L/2 \rfloor$

and the maximum lag and sample relation is $M = N - \lceil L/2 \rceil$. This lag product formation is the first step in taking a discrete Wigner Distribution [*Cohen*, 1995].

This specific type of lag product formation is detailed in [*Farley*, 1969a] and had been referred to as unbiased. This terminology does differ from what is used in statistic signal processing literature such as [*Shanmugan and Breipohl*, 1988] where the unbiased autocorrelation function estimate is carried out as so,

$$\hat{R}(m,l) = \frac{1}{L-l} \sum_{j=0}^{J-1} x(m - \lfloor l/2 \rfloor, j) x^*(m + \lceil l/2 \rceil, j). \tag{11}$$

With out the $\frac{1}{L-l}$ term the estimator will be windowed with a triangular function thus impacting the estimate of the ISR spectrum as this will act as a convolution in the frequency domain. This bias is taken into account in [*Farley*, 1969a] but it is simply wrapped up into the ambiguity function.

Applying a summation rule is usually the next step in creating an estimate of the autocorrelation function. This is done to get a constant range ambiguity across all of the lags for long pulse experiment[*Nygren*, 1996]. It also equalizes the statistics for each lag as the higher lags have greater variance.

An example summation rule for a forward product is shown in Figure 5. In the figure the image on the left is a basic representation of an ambiguity function of a long pulse. Its mirrored on the right with red bars which would show the integration area under it so the ambiguity function will be of equal size in range.

In the processing this is basically a summing of lags from different ranges. The amount of summing is similar to what is shown in Figure 5. There are a number of different summing rule each with their own trade offs [*Nygren*, 1996].

Lastly an estimate of the noise correlation is subtracted out of $\hat{R}(m,l)$, which is defined as $\hat{R}_w(m,l)$:

$$\hat{R}_w(m,l) = \sum_{j=0}^{J-1} w(m_w - \lfloor l/2 \rfloor, j) w^*(m_w + \lceil l/2 \rceil, j), \tag{12}$$

where $w(n_w)$ is the background noise process of the radar. Often the noise process is sampled during a calibration period for the radar when nothing is being emitted. The final estimate of the autocorrelation function after the noise subtraction and summation rule will be represented by $\hat{R}_f(m,l)$.

After the final estimation of the spectrum is complete the nonlinear least squares fitting takes place to determine the parameters. The basic class of nonlinear least-squares problems as seen in [*Kay*, 1993], are shown in Equation 13,

$$\hat{\mathbf{p}} = \underset{\mathbf{p}}{\operatorname{argmin}} (\mathbf{y} - \boldsymbol{\theta}(\mathbf{p}))^* \boldsymbol{\Sigma}^{-1} (\mathbf{y} - \boldsymbol{\theta}(\mathbf{p})). \tag{13}$$

In Equation 13, the data represented as $\mathbf{y}$ would be the final estimate of the autocorrelation function $\hat{R}_f(m,l)$ at a specific range or its spectrum $\hat{S}_f(m,\omega)$. The parameter vector $\mathbf{P}$ would be the plasma parameters N_e, T_e, T_i and various other parameters including ion velocities. The fit function $\boldsymbol{\theta}$ is the IS spectrum calculated from models, such as once seen in [*Kudeki and Milla*, 2011], smeared by the ambiguity function. In the case of the long pulse the ambiguity can be simply applied

by multiplying it with the autocorrelation function $R(l)$, if the summation rule is properly applied. The correlation matrix $\mathbf{\Sigma}$ is often realized as a diagonal matrix for many ISR systems the variance of the lags or each point of the spectrum being the values. The variance of the ACF estimator can be estimated using the following,

$$\sigma^2_{\hat{R}(l)} = \frac{1}{JL} \sum_{m=-(L-l-1)}^{L-l-1} \left(\frac{L-|m|+1}{L} \right) \left(|\hat{R}(m)|^2 + |\hat{R}(m+l)\hat{R}(m-l)| \right) + \hat{N}^2 \quad (14)$$

where N is the estimated noise power. To estimate the spectrum variance the matrix $\mathbf{\Sigma}$ is transformed in to the Fourier domain using FFTs (FFT on the columns and IFFT on the rows) so as to model the $\mathbf{F\Sigma F}^*$ matrix operation.

In the past ISR researchers have used the Levenberg-Marquart algorithm to fit data [*Nikoukar et al.*, 2008]. This specific iterative algorithm moves the parameter vector $\mathbf{p}$ by a perturbation $\mathbf{h}$ at each iteration[*Gavin*, 2013]. Specifically Levenberg-Marquart was designed to be a sort of meld between two different methods Gradient Decent, and Gauss-Newton. The perturbation vector $\mathbf{h}_{lm}$ can be calculated using the following:

$$\left[\mathbf{J}^T\mathbf{\Sigma}^{-1}\mathbf{J}\right]\mathbf{h}_{lm} = \mathbf{J}^T\mathbf{\Sigma}^{-1}(\mathbf{y} - \boldsymbol{\theta}(\mathbf{p})) \quad (15)$$

where $\mathbf{J}$ is the Jacobian matrix $\partial\boldsymbol{\theta}/\partial\mathbf{p}$ [*Levenberg*, 1944; *Marquardt*, 1963].

Using the scipy optimize tool box the fitted parameters can determined using the leastsquares function. This function outputs the fitted parameters along with a covariance matrix. This matrix is calculated using a numerical approximation to the

Jacobian matrix that the function uses to determine the solution. The Hessian, $\mathbf{H}$ is then calculated by using the Jacobian and then inverted to get the covariance matrix. Due to the way the numerical routines solve the problem this matrix must be multiplied by the error between the estimated parameters and the data,

$$\mathbf{\Sigma}_{\hat{\mathbf{p}}} = \frac{(\mathbf{J}^T\mathbf{J})^{-1}(\mathbf{y} - \boldsymbol{\theta}(\hat{\mathbf{p}}))^*\mathbf{\Sigma}^{-1}(\mathbf{y} - \boldsymbol{\theta}(\hat{\mathbf{p}}))}{L - N_{\mathbf{p}}}, \tag{16}$$

where $N_{\mathbf{p}}$ is the number of parameters being fit. The variances of the parameters are then taken as the diagonals of the matrix. Often though the Hessian matrix is undefined so it can not be inverted so the error term is then set as a NaN.

4. Simulation Examples

5. Conclusion

Acknowledgments. This work was supported by the National Science Foundation, through Aeronomy Program Grant AGS-1339500 to Boston University and Cooperative Agreement AGS-1242204 between the NSF and the Massachusetts Institute of Technology, and by the Air Force Office of Scientific Research under contract FA9550-12-1-018. The authors are grateful to the International Space Science Institute (ISSI, Bern, Switzerland) for sponsoring a series of workshops from which the idea for this work emerged.

Software used to create figures for this publications can be found at https://github.com/jswoboda/. Please contact the corresponding author, John Swo-

boda at swoboj@bu.edu, with any questions regarding the software along with any requests for the specific data used for the figures.

References

Butler, T. W., J. Semeter, C. J. Heinselman, and M. J. Nicolls (2010), Imaging f region drifts using monostatic phased-array incoherent scatter radar, *Radio Sci.*, *45*(5), RS5013, doi:10.1029/2010RS004364.

Cohen, L. (1995), *Time Frequency Analysis*, Prentice Hall.

Dahlgren, H., J. L. Semeter, K. Hosokawa, M. J. Nicolls, T. W. Butler, M. G. Johnsen, K. Shiokawa, and C. Heinselman (2012a), Direct three-dimensional imaging of polar ionospheric structures with the resolute bay incoherent scatter radar, *Geophysical Research Letters*, *39*(5), doi:10.1029/2012GL050895.

Dahlgren, H., G. W. Perry, J. L. Semeter, J. P. St. Maurice, K. Hosokawa, M. J. Nicolls, M. Greffen, K. Shiokawa, and C. Heinselman (2012b), Space-time variability of polar cap patches: Direct evidence for internal plasma structuring, *Journal of Geophysical Research: Space Physics*, *117*(A9), doi:10.1029/2012JA017961.

Diaz, M. A., J. L. Semeter, M. Oppenheim, and M. Zettergren (2008), Particle-in-cell simulation of the incoherent scatter radar spectrum, *Radio Science*, *43*(1), n/a–n/a.

Dougherty, J. P., and D. T. Farley (1960), A theory of incoherent scattering of radio waves by a plasma, *Proceedings of the Royal Society of London. Series A, Mathematical and Physical Sciences*, *259*(1296), pp. 79–99.

Dougherty, J. P., and D. T. Farley (1963), A theory of incoherent scattering of radio waves by a plasma, 3 scattering in a partly ionized gas, *Journal of Geophysical Research*, *68*, 5473.

Farley, D. T. (1969a), Incoherent scatter correlation function measurements, *Radio Sci.*, *4*(10), 935–953.

Farley, D. T. (1969b), Incoherent scatter power measurements; a comparison of various techniques, *Radio Sci.*, *4*(2), 139–142.

Farley, D. T., J. P. Dougherty, and D. W. Barron (1961), A theory of incoherent scattering of radio waves by a plasma ii. scattering in a magnetic field, *Proceedings of the Royal Society of London. Series A, Mathematical and Physical Sciences*, *263*(1313), pp. 238–258.

Gavin, H. P. (2013), The levenberg-marquardt method for nonlinear least squares curve-fitting problems.

Gordon, W. (1958), Incoherent scattering of radio waves by free electrons with applications to space exploration by radar, *Proceedings of the IRE*, *46*(11), 1824–1829, doi:10.1109/JRPROC.1958.286852.

Hagfors, T. (1961), Density fluctuations in a plasma in a magnetic field, with applications to the ionosphere, *Journal of Geophysical Research*, *66*(6), 1699–1712, doi:10.1029/JZ066i006p01699.

Hysell, D. L., F. S. Rodrigues, J. L. Chau, and J. D. Huba (2008), Full profile incoherent scatter analysis at jicamarca, *Annales Geophysicae*, *26*(1), 59–75, doi:10.5194/angeo-26-59-2008.

Kay, S. (1993), *Fundamentals of Statistical Signal Processing, Vol. I - Estimation Theory*, Prentice Hall.

Kudeki, E., and M. Milla (2011), Incoherent scatter spectral theories: Part i: A general framework and results for small magnetic aspect angles, *IEEE Transactions on Geoscience and Remote Sensing*, *49*(1), 315–328, doi:10.1109/TGRS.2010.2057252.

Levenberg, K. (1944), A method for the solution of certain non-linear problems in least squares, *Quarterly of Applied Mathematics*, *2*, 164–168.

Marquardt, D. W. (1963), An algorithm for least-squares estimation of nonlinear parmeters, *Journal of the Society for Industrial and Applied Mathematics*, *11*(2), 431–441.

Milla, M., and E. Kudeki (2011), Incoherent scatter spectral theories-part ii: Modeling the spectrum for modes propagating perpendicular to **b**, *IEEE Transactions on Geoscience and Remote Sensing*, *49*(1), 329–345, doi:10.1109/TGRS.2010.2057253.

Mitchell, R., and D. Mcpherson (1981), Generating nonstationary random sequences, *Aerospace and Electronic Systems, IEEE Transactions on*, *AES-17*(4), 553–560, doi:10.1109/TAES.1981.309184.

Nicolls, M. J., and C. J. Heinselman (2007), Three-dimensional measurements of traveling ionospheric disturbances with the Poker Flat Incoherent Scatter Radar, *Geophysical Research Letters*.

Nicolls, M. J., R. Cosgrove, and H. Bahcivan (2014), Estimating the vector electric field using monostatic, multibeam incoherent scatter radar measurements, *Radio Science*, *49*(11), 1124–1139, doi:10.1002/2014RS005519.

Nikoukar, R., F. Kamalabadi, E. Kudeki, and M. Sulzer (2008), An efficient near-optimal approach to incoherent scatter radar parameter estimation, *Radio Science*, *43*(5), doi:10.1029/2007RS003724.

Nygren, T. (1996), *Introduction to Incoherent Scatter Measurements*, Invers OY.

Semeter, J., C. J. Heinselman, G. G. Sivjee, H. U. Frey, and J. W. Bonnell (2005), Ionospheric response to wave-accelerated electrons at the poleward auroral boundary, *Journal of Geophysical Research*, *110*(A11), A11,310–13.

Semeter, J., T. Butler, C. Heinselman, M. Nicolls, J. Kelly, and D. Hampton (2009), Volumetric imaging of the auroral ionosphere: Initial results from pfisr, *Journal of Atmospheric and Solar-Terrestrial Physics*, *71*, 738 – 743, doi: 10.1016/j.jastp.2008.08.014.

Shanmugan, K. S., and A. M. Breipohl (1988), *Random Signals Detection Estimation and Data Analysis*, first ed., Wiley.

Swoboda, J., J. Semeter, and P. Erickson (2015), Space-time ambiguity functions for electronically scanned isr applications, *Radio Science*, *50*(5), 415–430, doi: 10.1002/2014RS005620.

Zettergren, M., and J. Semeter (2012), Ionospheric plasma transport and loss in auroral downward current regions, *J. Geophys. Res.*, *117*(A6), A06,306, doi: 10.1029/2012JA017637.

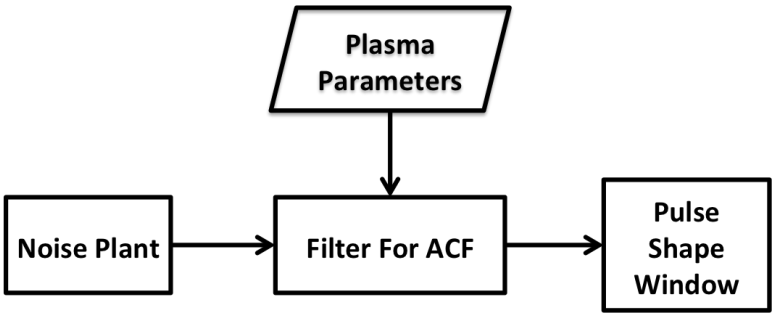

Figure 1. Diagram for I/Q simulator signal flow.

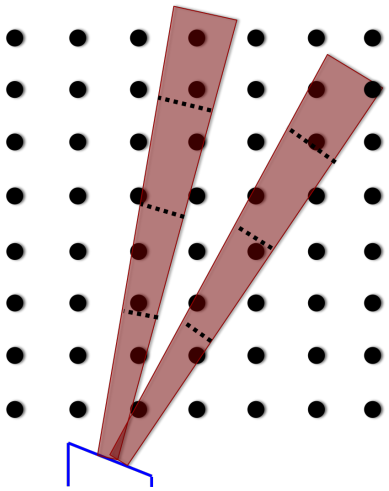

Figure 2. Beam Sampling Diagram

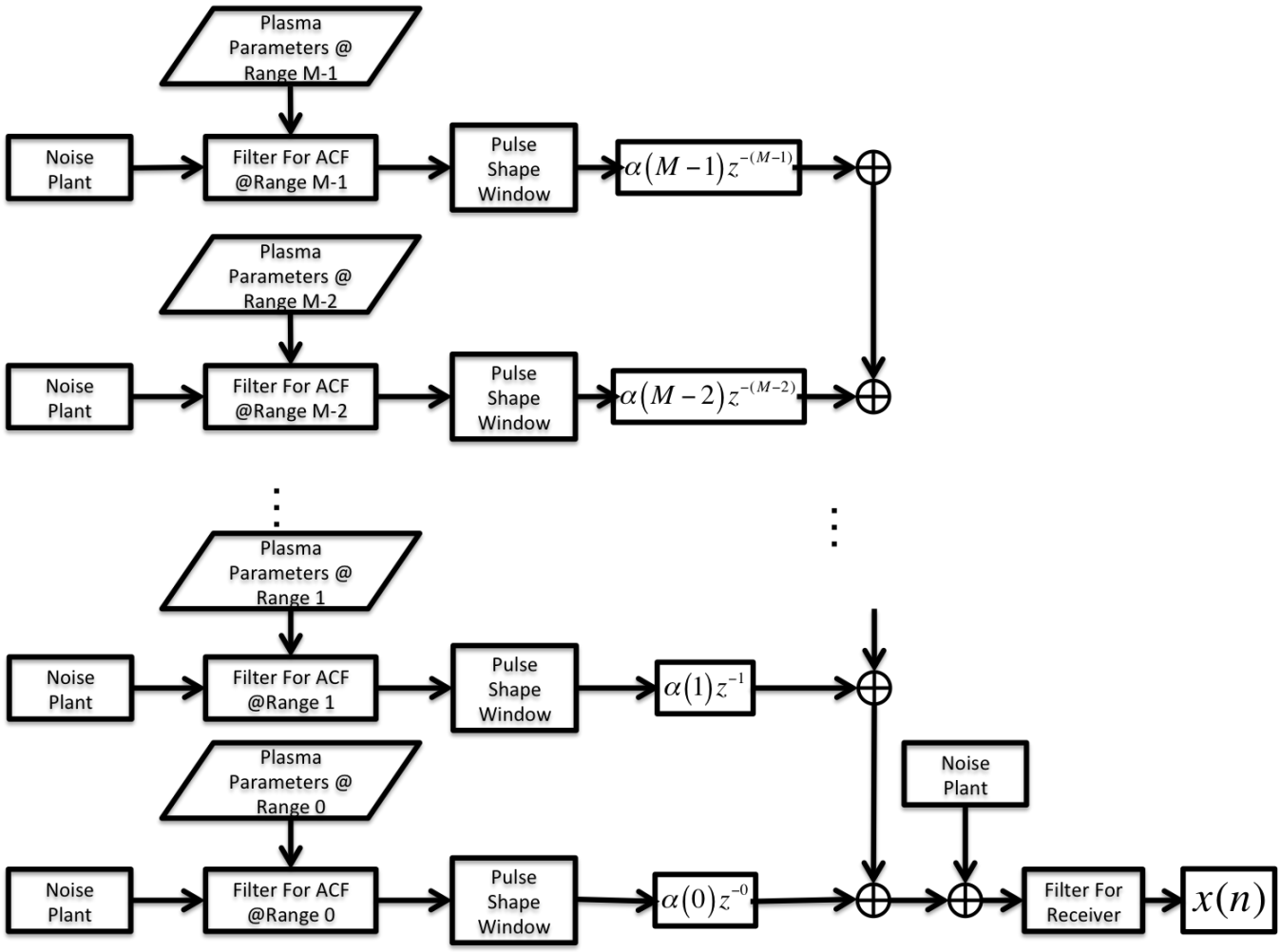

Figure 3. ISR Simulation Diagram

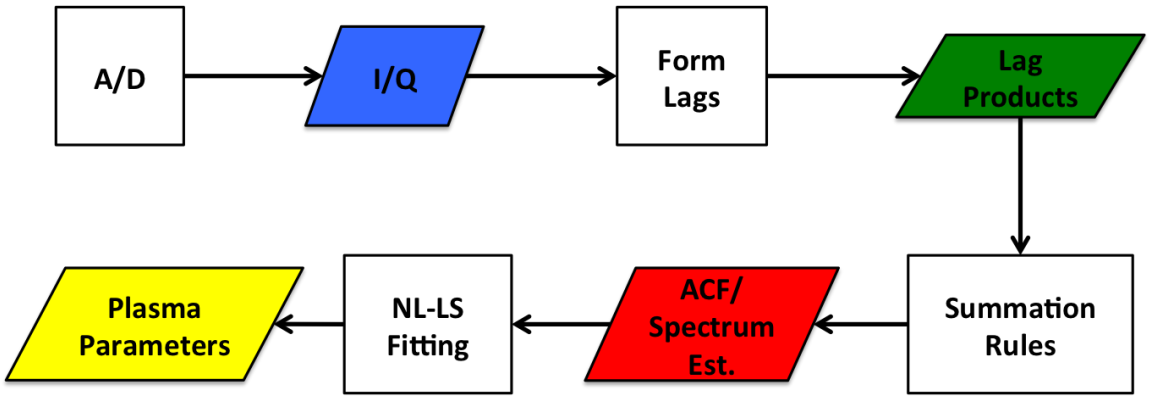

Figure 4. ISR signal processing chain, with signal processing operations as squares and data products as diamonds.

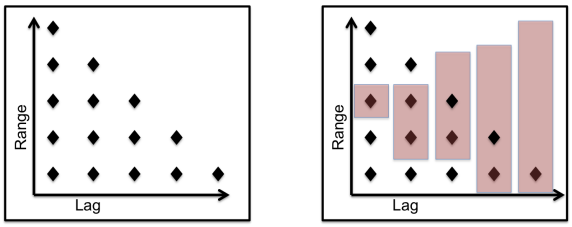

Figure 5. Summation Rule Diagram